IOP Publishing Plasma Physics and Controlled Fusion
Plasma Phys. Control. Fusion **62** (2020) 094002 (11pp) https://doi.org/10.1088/1361-6587/ab9b3b

Experimental evidence of electron-cyclotron current drive-based neoclassical tearing mode suppression threshold reduction during mode locking on DIII-D

A O Nelson[1,2], **N C Logan**[2], **W Choi**[2], **E J Strait**[3] and **E Kolemen**[1]

[1] Princeton University, Princeton, NJ 08544, United States of America
[2] Princeton Plasma Physics Laboratory, Princeton, NJ 08543, United States of America
[3] General Atomics, PO Box 85608, San Diego, CA 92 186-5608, United States of America

E-mail: ekolemen@pppl.gov

Received 28 February 2020, revised 26 May 2020
Accepted for publication 10 June 2020
Published 24 July 2020

Abstract
The repetitive locking-unlocking process of a large $m/n = 2/1$ neoclassical tearing mode (NTM) is studied on the DIII-D tokamak. Cyclical periods of partial suppression are achieved when β_p and the expected bootstrap current J_{BS} drop upon back-transitions to L-mode. Diminished L-mode bootstrap current is required to explain decreased island size as modeled by the generalized Rutherford equation. At EC power levels too low to fully suppress the NTM, partial suppression is enough to reduce the torque on the mode to the point where viscous drag from the background plasma overcomes the electromagnetic torque and restores fast plasma rotation and H-mode. Additional current drive is shown to further reduce the size of the mode until full suppression is achieved. These results suggest that the suppression of locked modes may be aided by the lower bootstrap current in L-mode plasmas, possibly improving chances of disruption avoidance in ITER.

Keywords: locked modes, bootstrap current, NTM, ECCD, tokamak

(Some figures may appear in colour only in the online journal)

1. Introduction

One of the performance-limiting concerns for tokamak reactors is the spontaneous development of undesired magnetohydrodynamic (MHD) instabilities. A common variety of MHD instability is the neoclassical tearing mode (NTM), which is a resistive tearing mode that leads to degradation in the plasma energy and angular momentum and can often set a limit on the total plasma beta [1–3]. NTMs are sustained by helical perturbations to the bootstrap current that occur in the vicinity of a mode rational surface (for example the $m/n = 2/1$ surface, where m is the poloidal mode-number and n is the toroidal mode-number.) Here the bootstrap current refers to the confinement-enhancing, self-generated current that results from pressure gradients and collisions in a toroidal geometry [4]. Importantly, the bootstrap current is usually larger in H-mode than in L-mode [5].

NTMs often originate when some small 'seed' island flattens a portion of the pressure profile due to fast parallel transport along magnetic field lines. Since the bootstrap current is proportional to the gradient of the pressure profile, the bootstrap current in the island region acquires a helical perturbation, encouraging the growth of the mode [3]. As a rotating 2/1 NTM grows, it will typically endure induction braking from any conducting surfaces near the plasma, such as a resistive wall [6–10]. If the wall drag is large enough, the mode can slow down until it is stationary in the laboratory frame, at which point it is identified as a locked mode

(LM). LMs frequently lead to large disruption events [11–13].

Since NTMs and LMs are strongly associated with performance degradation and the onset of disruptions, control and suppression of these modes is an important area of research. One of the most promising methods of NTM suppression is the application of co-current radio frequency (rf) power current drive at the mode rational surface. This is often accomplished through the use of localized electron-cyclotron current drive (ECCD) or electron-cyclotron heating (ECH). Not only does the application of ECCD to the mode rational surface increase the linear stability, but it is also able to drive additional plasma current through the island [14, 15]. This additional current effectively replaces the 'missing' bootstrap current at the mode rational surface and thereby reduces the destabilizing drive for the island.

While ECCD suppression of NTMs has been extensively demonstrated for both rotating [16, 17] and locked [18] modes, the necessary power P_{EC} can not always be achieved experimentally. This constraint may become more important in burning plasma scenarios, where any ECH power used for NTM mitigation must be diverted from heating the main plasma. In this work, the effects of insufficient heating power on a $m/n = 2/1$ magnetic mode are documented and explored, leading to insights on the locking and unlocking dynamics of large $n = 1$ NTMs. It is shown that while insufficient ECCD is unable to fully suppress a large NTM, disruptions may still be avoided through partial mitigation of the island size.

The rest of this paper is organized as follows. In section 2, the general experimental procedure, including a series of three shots on DIII-D with increasing P_{EC}, is outlined. Calculations of the island size and plasma rotation are presented in sections 3 and 4, respectively, along with a discussion of the locking and unlocking dynamics of the $n = 1$ mode. In these sections, the changing bootstrap current is shown to have a dramatic effect on the suppression of the LM. Concluding remarks are provided in section 5, suggesting that LMs may be easier to suppress after a back-transition to L-mode since the bootstrap current is smaller.

2. Experimental overview

Suppression of NTMs in DIII-D is routinely attempted via localized current drive with ECCD at power levels between $P_{EC} \sim$ 1–3 MW. This work focuses on the partial suppression of a large $m/n = 2/1$ tearing mode in a lower single-null plasma with the strike-line inside the closed divertor baffle. The three discharges shown in figure 1 are selected from a larger dataset in order to minimize variation in the background plasma state. The reference plasmas have q_0 near 1 with visible sawtooth oscillations, $q_{95} \sim$ 4.3, average triangularity $\delta \sim$ 0.5, elongation $\kappa \sim$ 1.3, are predominantly NBI heated ($P_{NBI}/P_{EC} \sim$ 1.3–2.1 with $P_{tot} \sim$ 5.5–6.8 MW) and were designed around a high-beta hybrid scenario with high current drive efficiency of central ECCD and consistent NTM triggering. The discharges were run with $I_p = 1.25$ MA and $B_t = -1.85$ T, with $\beta_p \sim 1$ and $\beta_n \sim 2$. During a test of the 'catch and subdue' algorithm for NTM suppression [19, 20], the ECCD system is aimed at the rational surface of the $n = 1$ mode with real-time steerable mirrors in order to achieve maximal suppression efficiency. The NTMs in this experiment are triggered by naturally occurring transient MHD events that have been identified as sawteeth and fishbone instabilities. After a mode appears, the ECCD system is turned on in an attempt to stabilize the instability, as is shown in figure 2.

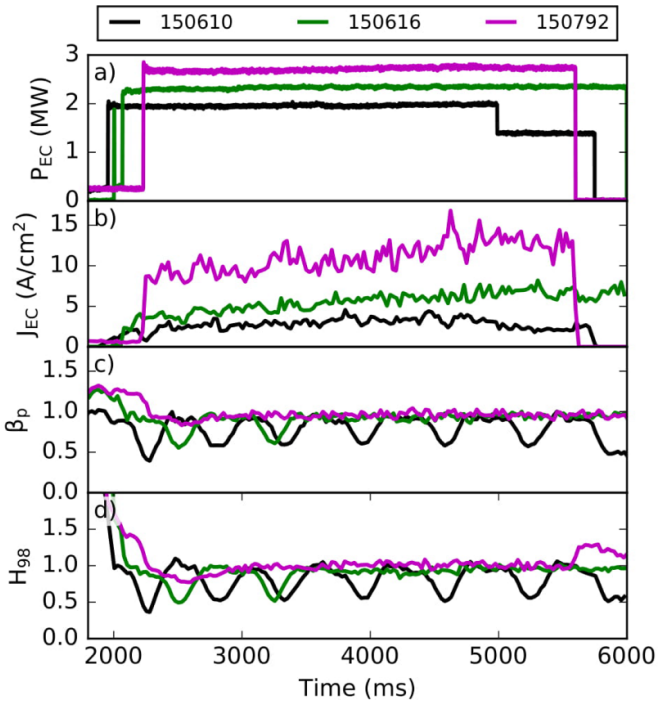

Figure 1. (a) P_{EC} is increased across DIII-D discharges 150 610 (black), 150 616 (green) and 150 792 (magenta). Also shown are (b) J_{EC} (c) β_p and (d) H_{98}.

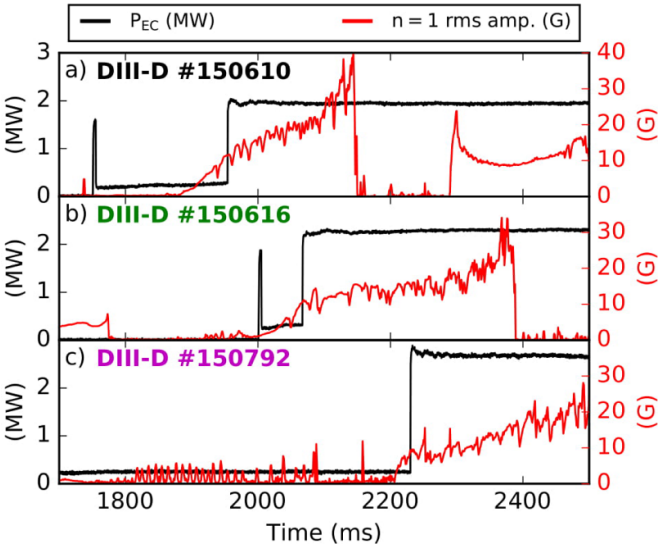

Figure 2. ECCD suppression of the NTMs begins shortly after the inital mode formation.

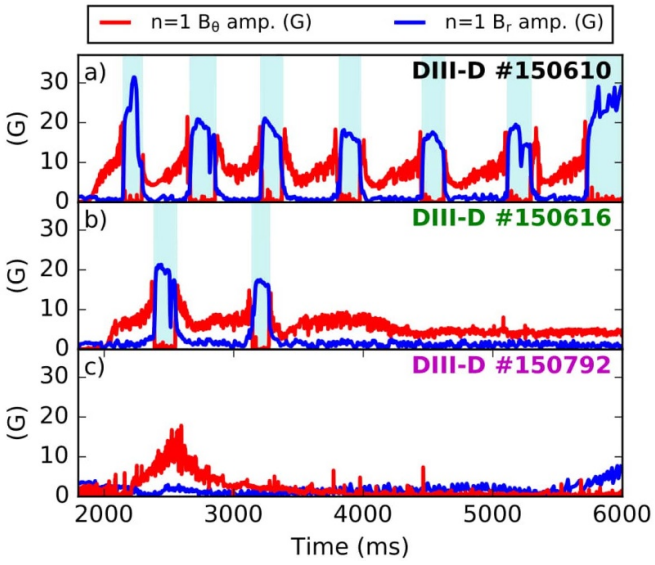

Figure 3. B_p and B_r for the three shots in figure 1. At low P_{EC} (a) the $n=1$ mode continuously oscillates between rotating (red) and locked states (blue), whereas at higher P_{EC} (c) the mode is suppressed before locking occurs. Times when the $n=1$ mode is locked are shaded throughout (cyan).

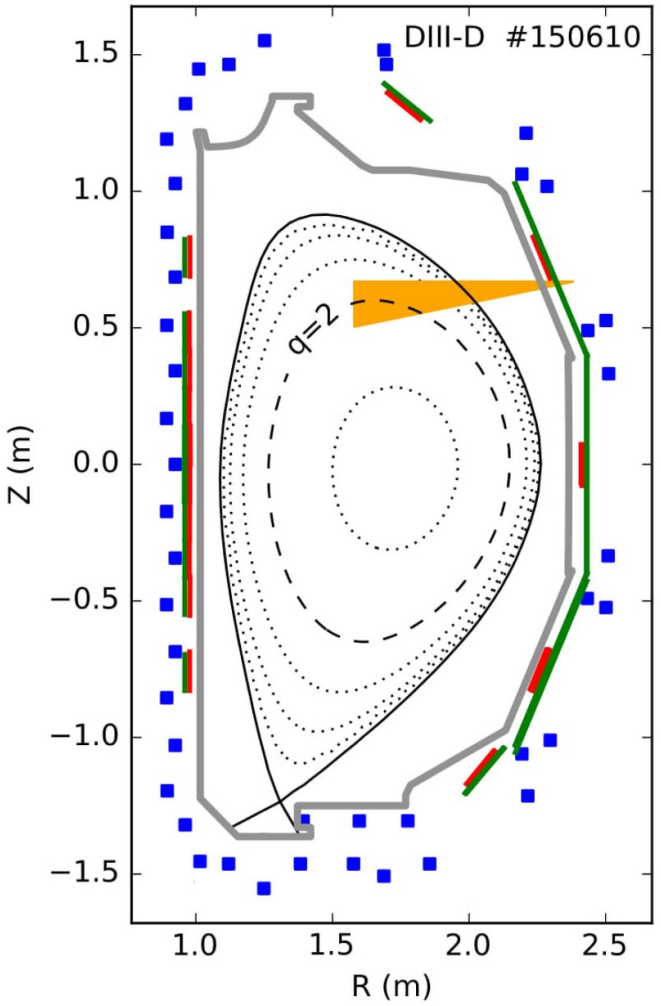

Figure 4. The magnetic geometry used in this experiment is shown, along with diagnostic locations for all of the available Mirnov probes (blue), B_p loops (red) and B_r loops. The ECCD trajectory (orange) is centered on the $q=2$ surface (dashed.) This setup was identical for all discharges considered here.

In the first discharge, the initially applied power $P_{EC} \sim 1.95\,MW$ is not sufficient to achieve full suppression of the $n=1$ mode, and is thus increased over a series of three shots (see figure 1(a)). At low power, an oscillatory locking/unlocking behavior is observed as the fast rotating $n=1$ mode is slowed and partially suppressed by the applied ECCD. This is shown in figure 3(a), where the rotating (B_θ) and locked (B_r) amplitudes of the $n=1$ mode are plotted in red and blue, respectively. Periods where the mode is locked are determined through rotation analysis in section 4 and are highlighted throughout this work in cyan. Note that, as discussed below, the modes are not fully stationary during the locked mode periods, instead showing slow rotation in response to torque balance with the plasma and the walls. The H-mode density for this discharge is $n \sim 4.4 \times 10^{19}\,m^{-3}$. After the ECCD power is turned off in this discharge, the LM grows without bound until the plasma disrupts.

Higher applied power $P_{EC} \sim 2.35\,MW$ leads to marginal mode suppression, with two locked-unlocked oscillations preceding partial mitigation of the $n=1$ mode. In this discharge, the deposited EC current density J_{EC} rises over the course of the discharge as the $q=2$ surface drifts inwards towards hotter plasma. The ECCD control scheme tracks this motion to ensure alignment with the tearing mode, and partial mitigation is eventually reached. For full suppression of the $n=1$ mode, a further increase in power to $P_{EC} \sim 2.75\,MW$ is required. At the highest power case, suppression of the $n=1$ mode is achieved before locking, as seen in figure 3(c). The majority of the analysis presented in this paper will focus on discharge #150 610, which has the lowest P_{EC} and shows the most consistent mode locking/unlocking behavior, though the increased suppression exhibited by the discharges with higher P_{EC} is also explained.

When the NTM is rotating, DC ECCD on the mode rational surface is averaged over the O-point and X-point. However, when the mode locks to the machine frame, applied ECCD can become localized at a specific phase relative to the island geometry. In order to fully suppress LMs, most state-of-the art methods use some variety of external phase control in order to align the O-point of the island to the ECCD deposition location. As has been shown in both theory [21, 22] and experiment [18, 23], island-suppression is most effective when ECCD is centered around the island O-point due to more effective replacement of the missing bootstrap current. In present LM suppression techniques, three-dimensional magnetic fields can be applied either to rotate the locked mode until the O-point is resonant with the ECCD deposition location [18, 24, 25] or to unlock and spin the mode at a desired frequency such that modulated ECCD can be applied to deposit current primarily in the island O-point [26, 27]. In this work, no such

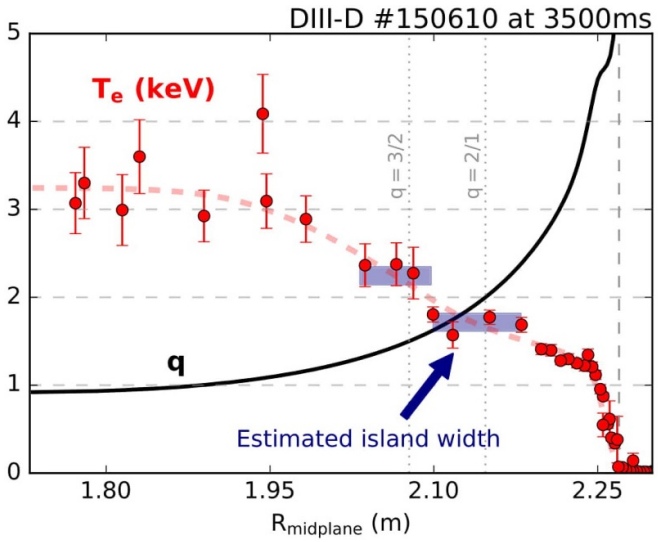

Figure 5. A typical electron temperature profile is shown as a function of major radius. Temperature flattening is observed in TS measurements at the locations of both islands.

efforts are made. The NTM is instead allowed to lock naturally to the machine error fields and, as a result, the island O-point, while slowly rotating, is generally around ~ 45 degrees out-of-phase with the ECCD deposition location. Alignment was checked manually during the locked times in discharges 150 610 and 150 616 and was found to be similar between all locked periods. Further, the slow rotation of the modes during the locked phases is reproducible between each locked phase. While the partial O-point/ECCD misalignment here is not optimized for suppression efficiency, it allows for partial mitigation of the LM and thus produces a natural mode unlocking event rather than full suppression or a disruption.

In each discharge in this experiment, the large $m/n = 2/1$ mode coexists with an $m/n = 3/2$ mode, as is often the case in DIII-D [28]. Both islands are large enough to flatten the local temperature gradient, as seen in figure 5. While the $n = 1$ mode exists outside of the available electron cyclotron emission (ECE) diagnostic coverage for these discharges, the $n = 2$ mode is well covered by ECE and can be detected with standard techniques [29]. The frequency of the $n = 2$ mode is measured to be exactly twice the frequency of the $n = 1$ mode throughout the discharge ($\omega^{3,2} = 2\omega^{2,1}$), suggesting that the large modes present here are subject to strong phase locking [30]. The coexistence of multiple LMs has been shown hasten the deterioration of thermal confinement and may be responsible for the quick collapse of the pedestal following locking events [31]. While comparable in size, the $n = 2$ mode is located inside the $q = 2$ surface so its magnetic signature in external measurements is partially screened by the $n = 1$ mode. Because of this, the analysis presented below focuses on the behavior of the $n = 1$ mode.

The remainder of this paper provides a discussion of the locking and unlocking dynamics for this series of discharges. Full advantage is taken of the detailed diagnostic suite available on DIII-D, including Thomson scattering (TS) [32], ECE [33], charge-exchange recombination spectroscopy (CER) [34], motional Stark effect polarimetry (MSE) [35] and a variety of magnetic diagnostics [36], in order to best assess the detailed physics processes occurring during the locking and unlocking events. An overview of the equilibrium geometry and available magnetic diagnostic locations is provided in figure 4. Poloidal and toroidal fits of the amplitude and phase of magnetic perturbations are accomplished with a least-squares SVD solution [37]. Raw magnetics data is detrended and bandpass filtered before fitting to remove noise and the finite toroidal and poloidal extent of the magnetic sensors on DIII-D is included in the sinusoidal fit basis functions. Fits are in good agreement with further analysis completed with the SLCONTOUR magnetic probe analysis routines at DIII-D [37]. The majority of the analysis presented here is conducted in the OMFIT framework [38].

3. Impact of L-mode on island size

After the $m/n = 2/1$ mode forms in discharge 150 610, it is allowed to grow for ~ 80 ms before the ECCD is turned on at 1954 ms. Upon the growth of the NTM, the confinement degradation is immediately visible with a drop of almost $\sim 70\%$ in H_{98} (see figure 1(d)). However, as noted above, the ECCD applied in this discharge is not sufficient to fully stabilize the mode. Plasma confinement continues to decrease as the mode locks, dropping to a minimum of $H_{98} \sim 0.54$. The additional transport caused by this large NTM and the associated confinement degradation is enough to trigger a back transition to L-mode after the mode locks. This is shown in figure 6, where the amplitude and frequency of the $n = 1$ are plotted along with the line-averaged-density and a representative D_α emission trace for two locking/unlocking cycles.

Interestingly, oscillations in the amplitude of the $n = 1$ mode are aligned with the L-H and H-L transitions rather than the locking/unlocking times. During the times when the plasma is in L-mode (depicted by the hatched red areas in figure 6), the $n = 1$ mode is shown to be decreasing in size. In contrast, the $n = 1$ mode increases in size when the plasma is in H-mode. This inspires an interesting hypothesis regarding the behavior of this mode, which we explore below in more depth. The initial formation, growth and locking of the $n = 1$ mode in this plasma causes significant confinement degradation such that H-mode is lost. However, as the plasma transitions back into L-mode, the *expected* bootstrap current drops as L-mode equilibria generally operate at lower J_{BS} due to having lower β_p. The ECCD-driven current J_{EC} is calculated with the ONETWO code [39, 40] and remains approximately constant during this period of time (see figure 1(b)). Thus the fraction of the missing bootstrap current that is replaced by ECCD (defined here as the bootstrap ratio $r_{BS} = J_{EC}/J_{BS}$) increases. Further, the drop of β_p in L-mode also directly increases the suppression efficiency of existing ECCD, as will be shown via the generalized Rutherford equation [3, 17]. The combination of these two effects yields better suppression of the $n = 1$ mode, which then decreases in size until confinement improves enough for the recovery of H-mode.

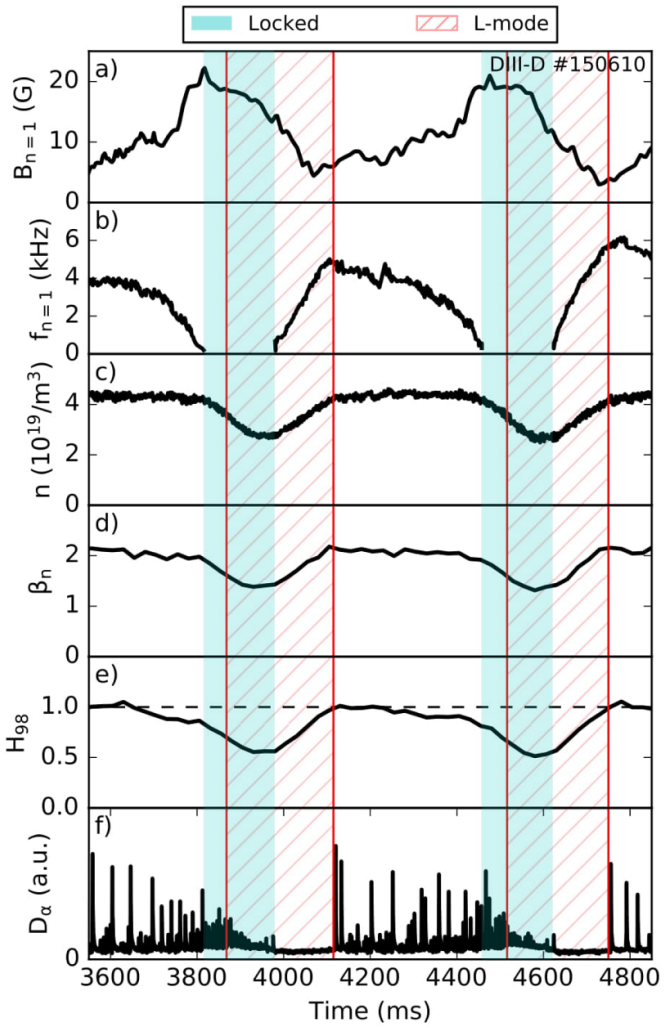

Figure 6. Amplitude (a) and frequency (b) of the $n = 1$ mode are shown alongside the line-averaged density (c), β_n (d), H_{98} (e) and a D_α signal (f) for DIII-D discharge 150 610. In this and future figures, the times during which the mode is locked (cyan, shaded) precede back-transitions to L-mode (red, hatched) by ~ 100 ms.

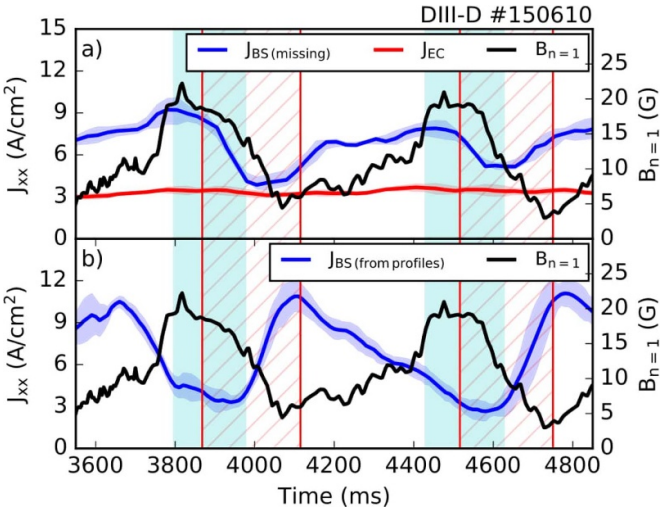

Figure 7. (a) The missing J_{BS} from ONETWO (blue) and J_{EC} (red) are compared as a function of time over two locking cycles. When the plasma is in L-mode, the missing J_{BS} drops to levels where J_{EC} can partially suppress the $n = 1$ mode, as seen by the decreasing $n = 1$ amplitude in L-mode (black). (b) J_{BS} calculated from experimentally measured profiles is shown to be inversely proportional to the $n = 1$ amplitude. As in figure 6, locked times are shaded in cyan and L-mode times are hatched in red.

For these discharges, the missing bootstrap current is calculated with ONETWO [41, 42]. This flux-surface-averaged calculation is consistent with the evolution of the poloidal magnetic field governed by Faraday's Law and includes the pressure and temperature gradient of each species. As is well established on DIII-D, the missing bootstrap current $J_{BS\,(missing)}$ calculated in the ONETWO code corresponds well to the missing bootstrap current in the plasma such that the mode becomes suppressed when $J_{EC} > J_{BS\,(missing)}$.

J_{EC} and $J_{BS\,(missing)}$ are compared as a function of time in figure 7(a). For clarity, only two cycles are shown here for in-depth analysis; the same behaviour to all cycles in this discharge except for the last, which ends in disruption after the ECCD is turned off. $J_{BS\,(missing)}$ in discharge 150 610 can be broadly characterized as oscillating between two states: a high-current state ($J_{BS\,(missing)} \approx 8$ A/cm^2) when the plasma is in H-mode, and a lower-current state with $J_{BS\,(missing)} \sim J_{EC}$ when the plasma is in L-mode. (L-mode times in figure 7(a) are shaded in red hatches.) When the plasma is in L-mode and the missing bootstrap current is low, the amplitude of the $n = 1$ mode is observed to decrease. This suggests a direct causal relationship between the bootstrap ratio r_{BS} and the growth of the $n = 1$, giving increased suppression of the island when the expected bootstrap current drops upon back transitions to L-mode. In this discharge $J_{BS\,(missing)} > J_{EC}$ at all times, so the $n = 1$ mode is never fully suppressed.

It is also possible to attempt a calculation of the bootstrap current at the $q = 2$ surface directly from the measured pressure profile according to

$$J_{BS} = -\frac{\sqrt{\epsilon}}{B_\theta}\frac{dp}{dr}, \qquad (1)$$

where $\varepsilon = r/R_0$ (the inverse aspect ratio), B_θ (the poloidal magnetic field), and dp/dr (the measured pressure gradient) are all evaluated at the $q = 2$ surface. While some bootstrap current can in principle exist within magnetic islands, in most large-island regimes $J_{BS} \equiv 0$ inside the island [43, 44]. However, due to flux-surface averaging and diagnostic orientation, it is rare to observe a completely flat pressure profile at the mode rational surface. As such, J_{BS} calculated from experimental pressure profiles using equation (1) is representative of the measured bootstrap current *in the vicinity* of the mode rational surface.

The measured bootstrap current $J_{BS\,(from\,profiles)}$ is plotted as a function of time in figure 7(b). In contrast to the missing bootstrap current from ONEWTWO, the local $J_{BS\,(from\,profiles)}$ is inversely proportional to $B_{n=1}$ throughout the discharge. Minimum values of $J_{BS\,(from\,profiles)}$ occur when the mode is locked. Note that the measured $J_{BS\,(from\,profiles)}$ never reaches zero because the TS and CER measurements used to reconstruct the pressure profile are not poloidally aligned with the

island O-point when the mode is locked. The inverse relationship between the local $J_{\mathrm{BS\,(from\,profiles)}}$ and the amplitude of the $n=1$ mode is in agreement with the expectation that the bootstrap current vanishes within larger islands: in this case, the larger the island, the flatter the averaged pressure profile near the $q=2$ surface and the lower the bootstrap current. The decrease of $J_{\mathrm{BS\,(from\,profiles)}}$ during the H-mode phase results from the fact that the mode is growing during this period, lowering $J_{\mathrm{BS\,(from\,profiles)}}$ from its maximum value at the L-H transition. Further, when J_{EC} is on the order of the missing bootstrap ($J_{\mathrm{BS\,(missing)}}$, figure 7(a)), the bootstrap current in the vicinity of the $q=2$ surface $J_{\mathrm{BS\,(from\,profiles)}}$ increases, showing effective replacement of the local bootstrap current via ECCD.

As seen in figure 7, both of these measurements show significant relationships between the bootstrap current and the mode size, as is expected for NTMs. The observation here that it is the magnitude of the *missing* bootstrap current rather than the local existing bootstrap current that is important for NTM suppression is characterized by the generalized Rutherford equation [3, 17, 45]. Including only the most relevant terms for this discussion, the generalized Rutherford equation can be written as

$$\frac{dw}{dt} \sim \Delta' r + f(w) * \beta_p - g(w) * \beta_p \left(\eta_{\mathrm{EC}} \delta_{\mathrm{EC}} \frac{J_{\mathrm{EC}}}{J_{\mathrm{BS}}} \right), \qquad (2)$$

where $f(w)$ and $g(w, \delta_{\mathrm{EC}})$ are functions of the island size w and the FWHM of the rf current drive δ_{EC}, among other parameters, and can be found in [46]. The effectiveness parameter η_{EC} can be written as $\eta_{\mathrm{EC}} = \eta_{\mathrm{EC}}(w, \delta_{\mathrm{EC}}, \Delta R)$ and accounts for misalignment ΔR in the J_{EC} deposition location.

Modeling of the island growth with the generalized Rutherford equation (section 3.1) confirms that both β_p and r_{BS} contribute to larger islands in H-mode. Incorporating a $\sim$ 30% rise in β_p from L- to H-mode is responsible for $\sim$ 60% of the observed island growth. In order to reproduce the full island size, however, the lower bootstrap ratio in H-mode needs to be taken into account as well. Changes in β_p and r_{BS} are both consequences of the L-H/H-L transitions, providing two separate factors that are both beneficial for NTM suppression in L-mode.

3.1. Deposition location vs. bootstrap ratio

When the $n=1$ mode locks to the machine frame and forces a back transition into L-mode, the density decay pushes the resonance location of the ECCD further inside the plasma relative to the mode resonant surface. The TORAY ray-tracing code [49] is used to model the ECCD deposition location as a function of time for discharge 150 610. The results, reproduced in figure 8, show that the peak ECCD deposition location moves inwards by $\rho \approx 0.06 \sim$ 6 cm from just outside the $q=2$ surface when the mode is rotating to just inside the $q=2$ surface when the mode is locked. Note further that the location of the $q=2$ surface is not strictly constant in time, but rather varies slightly as the plasma temperature and density change around the island location. Variations in plasma temperature and density may also be responsible for small changes in the amplitude of the driven current, but these are negligible compared to changes in the bootstrap current. Importantly, peak ECCD deposition location must be well-aligned with the mode resonant surface in order to achieve maximal suppression at a given P_{EC} [50, 51], so it is possible that the changing alignment between the ECCD deposition location and the $q=2$ rational surface had some effect on the suppression of the mode.

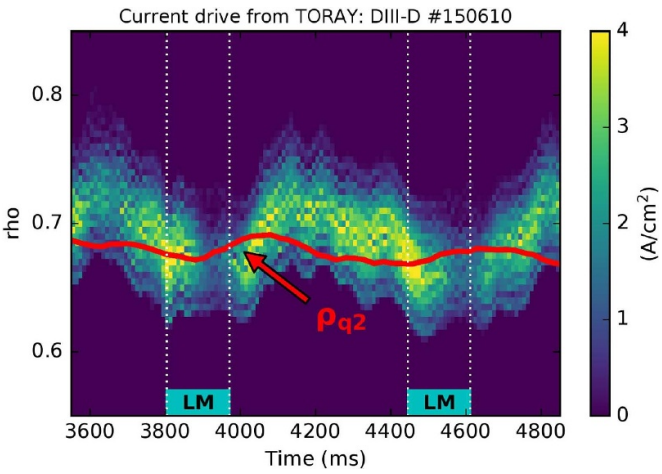

Figure 8. Current drive calculated as a function of ρ and time for DIII-D discharge 150 610. The location of the $q=2$ surface is overlayed in red.

In order to determine the relative importance of the shift in the ECCD deposition location, the generalized Rutherford equation in the form of equation (2) is solved using experimental parameters obtained at two representative times near the maximum and minimum mode sizes. Measured values for the maximum ECCD/NTM misalignment ($\Delta R \approx 4$ cm), β_p at the experimental island size ($\beta_p = 0.9 - 0.7$), and the bootstrap ratio ($r_{\mathrm{BS}} = 0.4 - 0.9$) are used in H-mode and L-mode, respectively. A value of $\Delta' = -1.25$ is assumed for both times in accordance with [17]. Furthermore, the pressure scale length is assumed to decrease linearly and β_p to increase with shrinking island size in order capture the effects of pressure peaking and fixed NBI power, respectively [17]. For comparison, the experimental island width is calculated separately during the rotating and locked phases of the discharge according to derivations in [47] and [48], respectively. Throughout the course of DIII-D discharge #150 610, the measured island width reaches a minimum of $\sim 5 \pm 1$ cm near the L-H transition and a maximum of $\sim 11 \pm 2$ cm near the H-L back transition, as seen in figure 9. Accounting for all effects, the island width predicted by the generalized Rutherford equation agrees with the measured island width in both L-mode and H-mode to within experimental error. As shown in figure 10, the island growth rate dw/dt is predominately influenced by changes in r_{BS} and β_p, demonstrating that the ECCD misalignment ΔR is not responsible for the oscillatory mode growth and suppression.

3.2. Increasing ECCD power

The increase in P_{EC} over the course of the three shots depicted in figure 1 predictably further stabilized the $n=1$ mode

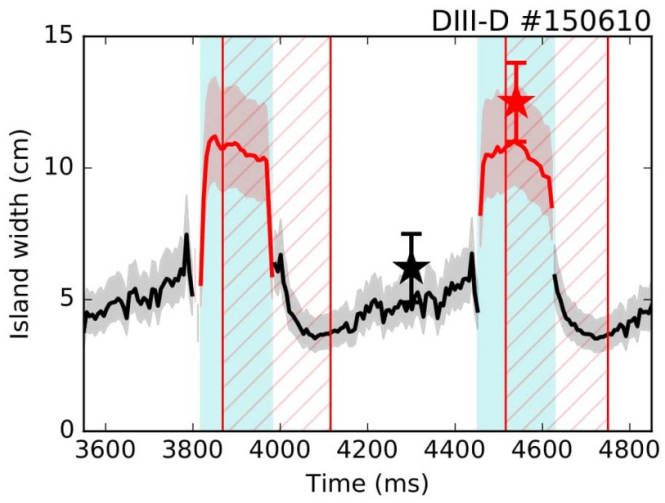

Figure 9. Island width as a function of time for the rotating (black, [47]) and the locked mode (red, [48]) phases. Representative calculations of the island width from the generalized Rutherford equation are shown as stars for both regimes.

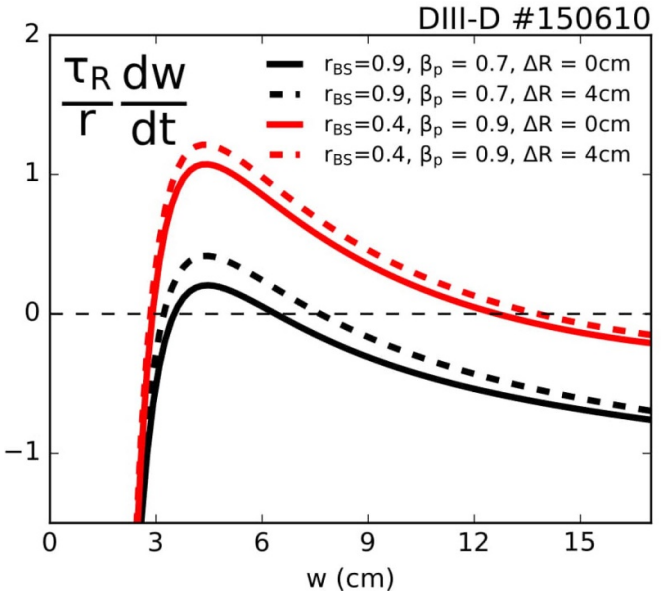

Figure 10. Solutions to the generalized Rutherford equation representing changes in ECCD alignment in L-mode (black) and H-mode (red). Smaller r_{BS} and larger β_p account for most of the island growth between the two states.

until full suppression before locking is achieved at $P_{EC} = 2.75$ MW. Of particular interest is the intermediate power level shown in figure 3(b), where the $n = 1$ went through two locking cycles before becoming partially mitigated as a quickly-rotating mode. In this case, while the injected rf power remained constant at $P_{EC} = 2.35$ MW, the driven current associated with ECCD deposition increased significantly over the course of the discharge from $J_{EC} \approx 3.6$ MA cm^{-2} at 2300 ms to $J_{EC} \approx 6.6$ MA cm^{-2} at 5300 ms (see figure 1(b)). The steady increase in J_{EC} in this case can be attributed to a slow inwards drift of the $q = 2$ surface, causing an increase in the plasma temperature at the ECCD deposition location. As J_{EC} becomes comparable to the bootstrap current at the $q = 2$ surface, the NTM is partially suppressed and reaches a steady-state condition at $H_{98} \sim 1$, permanently breaking the locking/unlocking cycle. In this manner the soft beta limit imposed by the NTM is reached before a destructive disruption event occurs.

4. Rotation dynamics

Since LMs are common precursors of disruptions, the slowing-down dynamics of NTMs have been studied in detail [6–10]. In general, when a fast rotating tearing mode first appears and is small, it rotates consistently with the background plasma. In the absence of resonant magnetic perturbations (RMPs), wall drag competes against viscous torque (and possibly NBI torque) to slow down the rotation as the mode grows. As it grows larger still, the wall drag becomes so large that the island slows to near zero and locks. Once locking occurs, however, the wall no longer applies any torque on the island. Instead, the error field comes into play and balances against the viscous drag of the background plasma rotation. After locking, an island can exhibit many different behaviors, including further growth and disruption. In the case discussed in this paper, the LM begins to shrink primarily due to ECCD suppression. The error field torque decreases with the shrinking island size until it is overpowered by the viscous torque exerted by background plasma and spin-up occurs.

Indeed, control of the torques exerted on NTMs has been used previously to excite locking/unlocking events. For example, RMPs can be used to create 3D fields that compete or overpower the error field. In [52], RMPs are used to exert an electromagnetic torque on the magnetic island that leads to velocity braking. With RMPs, a clear locking/unlocking hysteresis emerges with the RMP unlocking threshold significantly lower than the locking one. As the 3D field is reduced, the resonant torque decreases quicker than the viscous torque until torque balance is lost and mode spin-up is achieved [53, 54].

In DIII-D discharge 150 610, spin-up occurs naturally without any external magnetic control, offering a test of the established story stated above. Three distinct force balance states exist as the plasma oscillates between a locked L-mode condition and a fast-rotating H-mode condition. In the absence of RMPs, the torque balance dynamics of the island can be described by

$$\frac{dL}{dt} \sim T_{NBI} + T_{visc} + T_{EF} + T_{wall}, \tag{3}$$

where L is the angular momentum of the island, T_{NBI} is the torque on the island from NBI, T_{visc} is the viscous torque on the island from the background plasma, T_{EF} is torque from the the error fields, and T_{wall} is the electromagnetic torque from eddy currents in the wall [55]. Here we use $T_{visc} \sim L/\tau_\phi$, where τ_ϕ is an effective momentum confinement time, such that T_{visc} includes the effects of intrinsic torque [56]. It is important to note that T_{NBI} in equation (3) refers only to the NBI torque

deposited directly in the island, which is usually a small fraction of the total injected torque. The majority of the total injected NBI torque acts to drive rotation of the bulk plasma which then transfers momentum to the island via viscous drag.

When the island is small and in H-mode, it rotates quickly with the background plasma. In this case torques on the island are all small and we can write the force balance state as

$$\frac{dL}{dt} \sim (T_{\mathrm{NBI}} + T_{\mathrm{visc}}) + T_{\mathrm{wall}} \approx 0, \tag{4}$$

where the error field torque is negligible due to averaging during fast rotation. In the absence of large enough wall torques (for example with small islands), this state can continue indefinitely. However, as the island grows, T_{wall} begins to dominate and works to slow the island. In the contrasting state when a large mode is completely locked, the wall torque is replaced by error field torque such that

$$\frac{dL}{dt} \sim (T_{\mathrm{NBI}} + T_{\mathrm{visc}}) + T_{\mathrm{EF}} \approx 0 \tag{5}$$

It is important to note here that the error field depends on the position of the island. Thus the island will come to rest at the toroidal phase where the net torque described by equation (5) is zero. From this state, rotation can be recovered if the island becomes small enough that T_{EF} (which is a function of island size) becomes comparable with T_{visc}. At that point the viscous drag from even a slow-moving background plasma can be significant enough to prompt the recovery of fast rotation at the mode rational surface.

In the dynamic stages described by equation (3), a further simplification can be made near the locking/unlocking times. When the mode is large and rotating slowly, the island represents the dominant sink of momentum for the bulk plasma. In such a case, the viscous drag on the island from the bulk plasma is approximately equal to the total injected NBI torque given by T_{inj}. Even slow rotation ($\sim$ 10 Hz) can average out the error field torque, leaving the simplified expression

$$\frac{dL}{dt} \sim T_{\mathrm{inj}} + T_{\mathrm{wall}} \approx 0 \tag{6}$$

near the locking/unlocking times. This relationship is confirmed by experimental data [55] and is used here to determine the locking times and analyze the locking/unlocking dynamics.

In figure 11, torques calculated for a locking cycle with a single mode rotation are shown. T_{wall} is calculated from the Maxwell stress tensor [55, 57] using magnetic measurements from the low-field side of the machine and from the electromagnetic torque estimated using internal and external field decomposition [58]. The two calculations are in good agreement. Only the midplane sensors are included in this analysis; the poloidal extent of the mode is assumed to reach the boundary of the largest saddle loop detector. Further, due to the necessity of obtaining a baseline for all of the 3D magnetics in order to pick out small non-axisymmetric perturbations, the intrinsic error field has been removed from these calculations - leaving only the torque from eddy currents in the

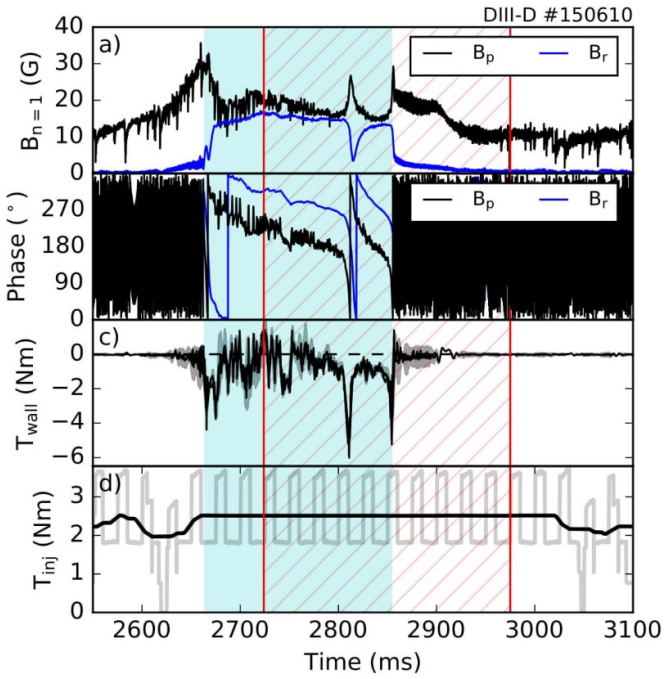

Figure 11. (a) B_{p} (black) and B_{r} (blue) of the $n = 1$ mode calculated with only outer midplane sensors. (b) Phases of the B_{p} (black) and B_{r} (blue) components of the $n = 1$ mode suggest locking to error fields. The electromagnetic torque T_{wall}(c) balances with the total NBI torque T_{inj} (d) during the locked times to halt the rotation of the mode.

wall. The electrical component of the Maxwell stress tensor is negligible at DIII-D-relevant frequencies and is ignored here.

In DIII-D tearing modes often rotate very slowly ($\sim$ few Hz) as 'quasi-stationary' modes in the counter-current direction despite continuous co-current NBI torque. The fast magnetics sensors used in figure 6(b) do not capture this slow motion, but drifts in the phase of the mode can be seen in figure 11(b). The phase of the 2/1 mode is nearly constant at $\sim 180^{\circ}$ when the plasma is locked and T_{wall} is low, consistent with locking to the error field as described by equation (5). In the selected time window the mode goes through a complete toroidal rotation at $t = 2812$ ms, creating significant T_{wall} in the process. As in [55], the locking and unlocking times can be determined by looking for peaks in T_{wall} that cancel external torque on the island. This state (described by equation (6)) can be seen in figure 11(c), where T_{wall} increases significantly at the beginning and end of the locked interval (cyan). Note that T_{inj} (figure 11(d)) is not held constant in these discharges but instead peaks when NBI programming attempts to match a requested beta target (between initial degradation of β_n at the onset of mode locking and the recovery of the target β_n at the the L-H transitions.)

After locking, a large NTM can, in general, manifest several different behaviors, including disruption and reversed rotation. Between the locking and unlocking events in this discharge, T_{wall} is small and the phase of the mode is nearly constant (the phase of B_{p} is $\sim 180^{\circ}$ for the majority of the locked phase.) This is consistent with locking to the error field as described by equation (5). A notable exception to this is

during the single slow rotation of the mode at $t = 2812$ ms. Note that the mode size, which decreases until the recovery of H-mode (see figure 6), continues to decrease even as T_{wall} grows during the initial recovery of fast rotation. Since the NBI torque is constant while the plasma is in L-mode, this suggests that the smaller island is eventually overpowered by viscous torque from the background plasma, leading to a recovery of fast mode rotation. T_{wall} spikes again as slow rotation is restored and the viscous torque begins to dominate. Throughout the LM period, the large electromagnetic torque caused by image currents works to resist the rotation of the LM, confirming the important role of the electromagnetic torque on influencing plasma rotation.

Stabilization of the large $n = 1$ modes in this experiment is predominantly influenced by larger r_{BS} and lower β_p in L-mode. As such, the island size continues to decrease even after an unlocking event until H-mode is eventually recovered. Mode unlocking, however, potentially has two additional effects that may help with the continued reduction in island size. First, unlocking eliminates any drive from the residual error fields [9]. This drive, which can couple to LMs, is canceled to zeroth order by the rotational averaging experienced by a rotating NTM. Second, eddy currents in the wall may also be partially stabilizing to the rotating tearing mode [9, 59]. Previous work has shown that a sufficiently small rotating island can be completely stabilized by interaction with a static external magnetic field, suggesting that mode unlocking can potentially further contribute to island suppression. However, in the context of the arguments made in section 3, the most important factor for aiding the suppression of an NTM remains the advantage of low β_p and higher r_{BS} in L-mode. After the appearance of a locked mode forces an H-L back transition due to confinement degradation, it is thus plausible to wish to extend this L-mode phase until the island is fully suppressed. In this scenario, potential reduction of injected NBI power after an H-L back transition could have the beneficial effect of prolonging the L-mode period, allowing for full mode suppression before high-energy H-mode can be safely recovered.

Although not considered in this experiment, the addition of RMPs can further change the torque balance dynamics. Adding an additional torque through rotating RMPs could help to slow the rotation recovery and keep the mode in a slowly rotating (entrained) state [27, 54]. This necessarily invokes a new torque balance state characterized by the addition of an RMP torque term T_{RMP} to equation (3). Controlled mode rotation at low frequencies ($\sim$ 10 Hz) could be combined with modulated ECCD at the same frequency to enable repetitive ECCD deposition at the island O-point. Modulated ECCD has been shown to enhance the NTM stabilization efficiency [26], and could help reduce the time required to fully suppress the island. Recent work indicated that RMPs can have significant influence on the suppressability of LMs with effects that vary depending on the RMP size and the bootstrap fraction [60]. Such effects should be considered when designing LM suppression schemes for future machines.

5. Discussion and conclusion

In the discharges presented above, a large $m/n = 2/1$ NTM is shown to go through repeated locking and unlocking events without external intervention through applied three-dimensional fields. When the mode locks, the plasma confinement is degraded to the point where a back transition to L-mode occurs. At constant P_{EC}, the bootstrap ratio $r_{\text{BS}} = J_{\text{EC}}/J_{\text{BS}}$ is modified as the denominator rises and falls in H-mode and L-mode, respectively. Larger r_{BS} combines with lower β_p to produce better suppression of the NTM, leading to mode mitigation in the L-mode plasmas. Smaller r_{BS} and higher β_p in H-mode contribute to mode growth. At a P_{EC} too low for full mode suppression and without any phase control of the locked island, disruptions are avoided in L-mode by partial suppression of the LM. The mode is shown to shrink to the point where viscous drag from the background plasma rotation can overcome the error field torque, causing an unlocking event and a recovery of H-mode.

The process detailed above on DIII-D holds some good news for disruption avoidance in ITER, which is of critical importance for safe operation of the machine. In general, studies on the suppression of NTMs on ITER have focused on achieving suppression before the mode locks [61–64]. However, due to the comparable mode growth and mode locking timescales on ITER, the requirement of full suppression before locking puts stringent requirements on the engineering design of mode control actuators [61–63, 65]. The predicted locking time on ITER is somewhere between $\sim 5 - 10$ s [64] whereas the full quench time is variable, but typically on the order of a few mode growth times ($\lesssim 10$ s) [66]. Since the NTM and LM onset thresholds fall significantly as rotation is reduced [67], LM avoidance is a major concern for ITER. Recent work has demonstrated the ability to deal with and suppress modes after they become locked, and will be extended towards implementation on ITER [18, 54]. However, suppression of LMs on ITER remains a difficult problem, and a full assessment of the benefits, drawbacks and complications of detailed suppression strategies is outside the scope of this paper and will require further study.

One of the biggest obstacles towards the suppression of these dangerous modes is the potential inaccessibility of enough P_{EC} to achieve full suppression, especially when significant ECCD is required to sustain the energy producing H-mode. While full suppression in H-mode is of course preferable, it remains plausible in the context of this work that, should a back-transition to L-mode occur, even partial suppression could be adequate to slow the growth of a LM to the point where additional actions could be taken before a catastrophic disruption event. Temporary loss of H-mode and subsequent mode suppression is a preferable alternative to immediate disruptions. In a study of more than 22 000 DIII-D discharges, the most common survival time of a LM before

disrupting is found to be ~ 300 ms, which is longer than the full L-mode stabilization times observed in this study [13]. In this context, the loss of H-mode upon mode locking could be beneficial in attempts to suppress LMs due to the diminished expected bootstrap current and the lower β_p that accompany a back transition to L-mode. These effects are realizable on typical mode suppression timescales. Additionally, the beneficial trends observed in this study could potentially be achieved through means other than H-L transitions: for example, diminished β_p can also be achieved through P_{NBI} control. Finally, suppression of LMs could be further assisted by non-linear effects such as current condensation, which is predicted to increase the efficiency of ECCD in very large islands (LMs) [68, 69].

A full analysis of the benefits and drawbacks of these techniques in terms of the relative importance of mode suppression and fusion gain will be the subject of future work. For example, maintaining burning plasma conditions and mitigating impurity influx from the tungsten wall must be assessed relative to easier mode suppression in L-mode. Likely, suppression in L-mode should be used only when initial suppression attempts fail, yielding more time to suppress the mode before a disruption occurs. While the additional effects discussed here do not provide a certain solution to the problem of mode suppression on ITER, they do broaden the scope of the problem to include potentially beneficial feedback mechanisms that could play a vital role in disruption mitigation.

Acknowledgments

The authors would like to thank Erik Olofsson for helpful discussions. Part of data analysis for this work was performed using the OMFIT integrated modeling framework [38, 70]. This material is based upon work supported by the U.S. Department of Energy, Office of Science, Office of Fusion Energy Sciences, using the DIII-D National Fusion Facility, a DOE Office of Science user facility, under Awards DE-AC02-09CH11466, DE-SC0015480, DE-SC0015878 and DE-FC02-04ER54698.

Disclaimer

ORCID iDs

A O Nelson https://orcid.org/0000-0002-9612-1936
N C Logan https://orcid.org/0000-0002-3268-7359
W Choi https://orcid.org/0000-0002-6891-2300
E Kolemen https://orcid.org/0000-0003-4212-3247

References

[1] Sauter O *et al* 1997 *Phys. Plasmas* **4** 1654–64
[2] Buttery R *et al* 2000 *Plasma Phys. Control. Fusion* **42** B61
[3] La Haye R J 2006 *Phys. Plasmas* **13** 055501
[4] Bickerton R J *et al* 1971 *Nature* **229** 110
[5] Chatthong B *et al* 2016 *Nucl. Fusion* **56** 016010
[6] Nave M F F *et al* 1990 *Nucl. Fusion* **30** 2575
[7] Zohm H *et al* 1990 *Europhys. Lett.* **11** 745–50
[8] Hender T C *et al* 1992 *Nucl. Fusion* **32** 2091
[9] Fitzpatrick R 1993 *Nucl. Fusion* **33** 1049
[10] Fitzpatrick R 1998 *Phys. Plasmas* **5** 3325
[11] Sykes A *et al* 1980 *Phys. Rev. Lett.* **44** 18
[12] Morris A W 1992 *Plasma Phys. Control. Fusion* **34** 1871
[13] Sweeney R *et al* 2017 *Nucl. Fusion* **57** 016019
[14] Fisch N J 1987 *Rev. Mod. Phys.* **59** 175
[15] Prater R 2004 *Phys. Plasmas* **11** 2349
[16] Gantenbein G *et al* 2000 *Phys. Rev. Lett.* **85** 1242
[17] Petty C C *et al* 2004 *Nucl. Fusion* **44** 243
[18] Volpe F A *et al* 2015 *Phys. Rev. Lett.* **115** 175002
[19] Kolemen E *et al* 2013 *Fusion Eng. Des.* **88** 2757–60
[20] Kolemen E *et al* 2014 *Nucl. Fusion* **54** 073020
[21] Hegna C C *et al* 1997 *Phys. Plasmas* **4** 2940
[22] De Lazzari D *et al* 2011 *Plasma Phys. Control. Fusion* **53** 035020
[23] Westerhof E *et al* 2007 *Nucl. Fusion* **47** 85–90
[24] Yu Q *et al* 2008 *Nucl. Fusion* **48** 065004
[25] Olofsson K E *et al* 2016 *Plasma Phys. Control. Fusion* **58** 045008
[26] Maraschek M *et al* 2007 *Phys. Rev. Lett.* **98** 025005
[27] Choi W *et al* 2018 *Nucl. Fusion* **58** 036022
[28] Hender T C *et al* 2004 *Nucl. Fusion* **44** 788
[29] Nelson A O *et al* 2019 *Plasma Phys. Control. Fusion* **61** 085013
[30] Fitzpatrick R 2015 *Phys. Plasmas* **22** 042514
[31] Hu Q *et al* 2019 *Nucl. Fusion* **59** 016005
[32] Carlstrom T N *et al* 1992 *Rev. Sci. Instrum.* **63** 4901
[33] Austin M E *et al* 2003 *Rev. Sci. Instrum.* **74** 1457
[34] Chrystal C *et al* 2012 *Rev. Sci. Instrum.* **83** 10D501
[35] Wróblewski D *et al* 1990 *Rev. Sci. Instrum.* **61** 3552
[36] Strait E J 2006 *Rev. Sci. Instrum.* **77** 023502
[37] Strait E J *et al* 2016 *Rev. Sci. Instrum.* **87** 11D423
[38] Meneghini O *et al* 2015 *Nucl. Fusion* **55** 083008
[39] Pfeiffer W W *et al* 1980 *San Diego, CA: General Atomics* **GA-A16178** Rep GA–A16178 https://ui.adsabs.harvard.edu/abs/1980occm.rept.....P/abstract
[40] St John H *et al* 1994 *Plasma Phys. Control. Nuclear Fusion Res.* **3** 603
[41] Sauter O *et al* 1999 *Phys. Plasmas* **6** 2834
[42] Sauter O *et al* 2002 *Phys. Plasmas* **9** 5140
[43] Fitzpatrick R 1995 *Phys. Plasmas* **2** 825–38
[44] Dong G *et al* 2017 *Nucl. Fusion* **57** 036009
[45] Westerhof E *et al* 2016 *Nucl. Fusion* **56** 036016
[46] La Haye R J *et al* 2002 *Phys. Plasmas* **9** 2051
[47] Shi T *et al* 2013 *Plasma Phys. Control. Fusion* **55** 055007
[48] Shiraki D *et al* 2014 *Nucl. Fusion* **54** 033006
[49] Prater R *et al* 2008 *Nucl. Fusion* **48** 035006
[50] La Haye R J *et al* 2008 *Nucl. Fusion* **48** 054004
[51] Nelson A O *et al* 2019 *Fusion Eng. Des.* **141** 25–9

[52] Frassinetti L *et al* 2014 *Plasma Phys. Control. Fusion* **56** 104001
[53] Shiraki D *et al* 2015 *Plasma Phys. Control. Fusion* **57** 025016
[54] Okabayashi M *et al* 2017 *Nucl. Fusion* **57** 016035
[55] Logan N C *et al* 2010 *Plasma Phys. Control. Fusion* **52** 045013
[56] Solomon W M *et al* 2009 *Nucl. Fusion* **49** 085005
[57] Hutchinson I H 2001 *Plasma Phys. Control. Fusion* **43** 145
[58] Sweeney R M *et al* 2019 *Phys. Plasmas* **26** 012509
[59] de Vries P C *et al* 1996 *Plasma Phys. Control. Fusion* **38** 467
[60] Tang W *et al* 2019 *Plasma Science and Technology* **21** 065103
[61] Ramponi G *et al* 1999 *Phys. Plasmas* **6** 3561
[62] La Haye R J *et al Nucl. Fusion* **49** 045005
[63] Van Den Brand H 2012 *Plasma Phys. Control. Fusion* **54** 094003
[64] Poli F M *et al* 2018 *Nucl. Fusion* **58** 016007
[65] Poli E *et al* 2015 *Nucl. Fusion* **55** 013023
[66] Lazzaro E *et al* 2018 *Plasma Phys. Control. Fusion* **60** 014044
[67] Buttery R J *et al* 2008 *Phys. Plasmas* **15** 056115
[68] Reiman A H *et al* 2018 *Phys. Rev. Lett.* **121** 225001
[69] Rodríguez E *et al* 2019 *Phys. Plasmas* **26** 092511
[70] Logan N C *et al* 2018 *Fusion Sci. Technol.* **74** 125–34